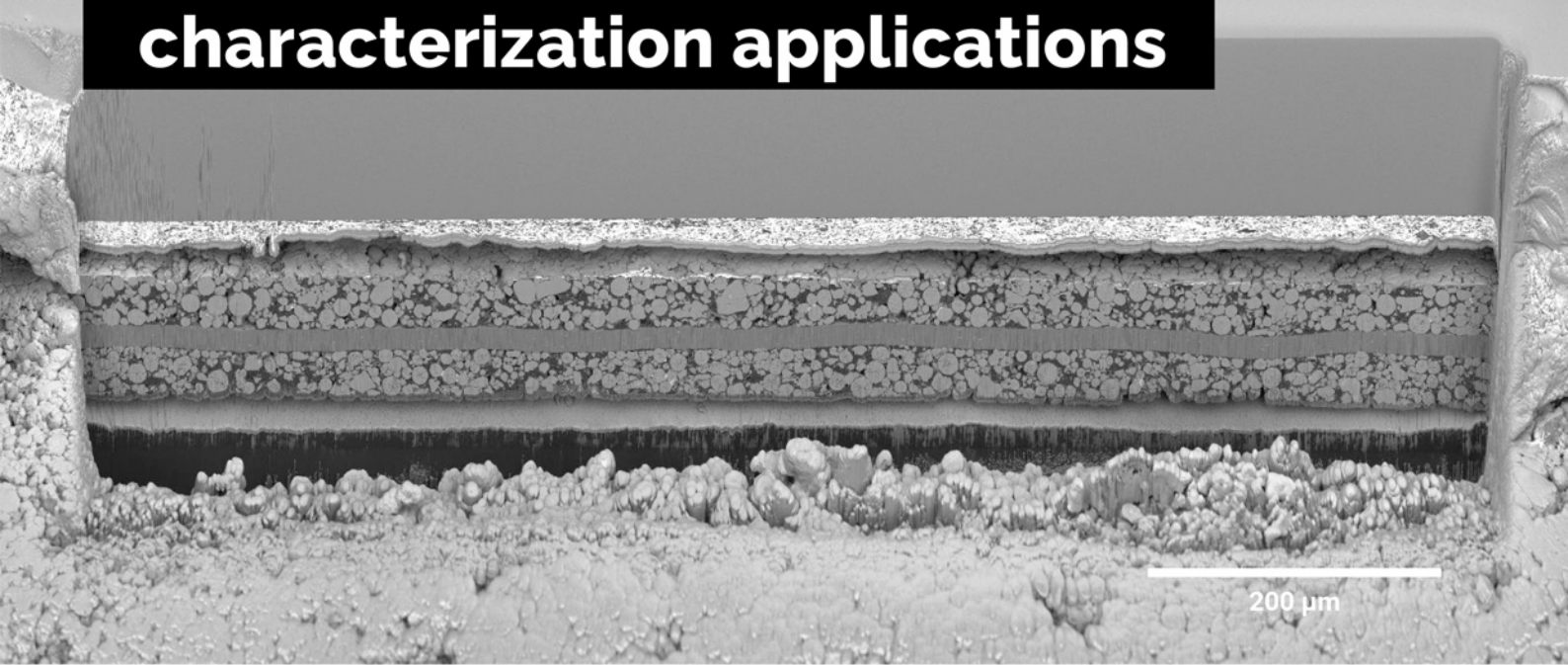


A unique combination of Plasma FIB and field-free UHR SEM for the widest range of multiscale materials characterization applications



1 mm cross-section through a Li-ion battery electrode

TESCAN AMBER X

- ✓ High throughput, large area FIB milling up to 1 mm
- ✓ Ga-free microsample preparation
- ✓ Ultra-high resolution, field-free FE-SEM imaging and analysis
- ✓ In-column SE and BSE detection
- ✓ Spot optimization for high-throughput, multi-modal FIB-SEM tomography
- ✓ Superior field of view for easy navigation
- ✓ Essence™ easy-to-use, modular graphical user interface



For more information visit

www.tescan.com

Environmental Self-Adaptive Wind Energy Harvesting Technology for Self-Powered System by Triboelectric-Electromagnetic Hybridized Nanogenerator with Dual-Channel Power Management Topology

Shun Yong, Hanqing Wang, Zenan Lin, Xiaosa Li, Boyu Zhu, Lijun Yang, Wenbo Ding,* Ruijin Liao, Jiyu Wang,* and Zhong Lin Wang*

Natural wind energy harvesting enables a far-reaching and sustainable solution to supply pervasive sensors in the Internet of Things (IoT). Electromagnetic generators (EMGs) struggle to harvest energy from breezes, which causes regrettable energy wastage. Herein, a triboelectric-electromagnetic hybridized nanogenerator (TEHG) is designed with a dual-rotor structure to consolidate harvesting band for high efficiency of triboelectric nanogenerators (TEGs) in breeze and the EMG in high wind speeds. The TEHG performs an efficient energy collection (41.05 W m^{-3}) and a smooth output in the wind speed of $2\text{--}16 \text{ m s}^{-1}$, attributed to the environmental self-adaptive cooperation between TENGs and EMGs. The TENG output power contribution is more than 70% at low wind speeds ($<5 \text{ m s}^{-1}$). Moreover, a dual-channel power management topology (DcPMT) is established to co-manage outputs of two modules in TEHG. By virtue of the DcPMT hierarchically combining the isolated storage with undervoltage lockout strategy, the TEHG steadily supplies a standardized 3.3 V voltage for commercial electronics. Furthermore, a TEHG-based self-powered system is demonstrated for driving sensors to monitor meteorological information. The TEHG with DcPMT is advantageous in broad-band and high-efficiency of wind energy harvesting, thus exhibiting a great potential for elevating the environmental self-adaptability and stability margin of the IoT.

1. Introduction

Trillions of sensors are envisioned with the pervasive interconnection as the cornerstone of the modern Internet of Things (IoT), supporting the digital links that could span human intelligent life.^[1–6] Realistically, the challenge of long-term, stable, and maintenance-free energy supply for massive sensors in the IoT definitely exerts a critical bottleneck role.^[7] The IoT sensors with the features of random and disordered distribution,^[8,9] could be powered by utilizing the eco-friendly and sustainable energy collection technologies especially natural wind energy harvesting, rather than conventional centralized generators.^[10–13] Traditionally, natural wind energy is mainly captured by using fan blades of turbines to convert wind energy into mechanical energy, which is then generated by electromagnetic generators (EMGs).^[14] However, within the limits of the armature winding coefficient and the magnetic flux density,

S. Yong, H. Wang, B. Zhu, L. Yang, R. Liao, J. Wang
State Key Laboratory of Power Transmission Equipment and System
Security and New Technology
Chongqing University
Shapingba, Chongqing 400044, P. R. China
E-mail: jiyuwang@cqu.edu.cn

Z. Lin, X. Li, W. Ding, J. Wang
Tsinghua-Berkeley Shenzhen Institute
Tsinghua Shenzhen International Graduate School
Tsinghua University
Beijing 518055, P. R. China
E-mail: ding.wenbo@sz.tsinghua.edu.cn

Z. L. Wang
Beijing Institute of Nanoenergy and Nanosystems
Chinese Academy of Sciences
National Center for Nanoscience and Technology (NCNST)
Beijing 100083, P. R. China
E-mail: zhong.wang@mse.gatech.edu

Z. L. Wang
CUSPEA Institute of Technology
Wenzhou, Zhejiang 325024, P. R. China

Z. L. Wang
School of Material Science and Engineering
Georgia Institute of Technology
Atlanta, GA 30332, USA

 The ORCID identification number(s) for the author(s) of this article can be found under <https://doi.org/10.1002/aenm.202202469>.

DOI: 10.1002/aenm.202202469

the operation of EMG requires a strong and stable wind speed (usually $>4\text{--}6\text{ m s}^{-1}$), resulting in a wind turbine falling in start or being interrupted when wind speed is frequently fluctuating or below the start-up wind speed, leading to a significant reduction in the efficiency of wind energy harvesting.^[14] More significantly, the global average wind speed at the observation altitude of 10 m is reported to be only 3.28 m s^{-1} ,^[10,15] implicating an insufficient utilization of most current wind turbines for a huge amount of breeze energy. Therefore, to fill in the gaps in breeze energy collection and dampen avoidable energy wastage, more advanced broad-band wind energy harvesting technologies are desirable to be further developed.

In the last decade, triboelectric nanogenerators (TENGs), based on the coupling of triboelectrification and electrostatic induction, are increasingly considered as a promising environmental energy harvesting technology due to its high efficiency and sensitive response especially for low-frequency energy harvesting.^[16–19] Up till now, TENGs have been widely applied to scavenge the low-frequency mechanical energy such as human biological energy, environmental vibration energy, water wave energy, and wind energy.^[20–25] Mechanism-wise, the TENG is suitable for harvesting low-speed wind energy while its energy conversion efficiency is inferior to EMG at high-speed winds. Considerable research recently report diverse hybrid strategies to address the limitation of any single harvesting method, dedicating to broadening wind speed range and enhancing wind energy harvesting efficiency with the complementary output characteristics of TENGs and EMGs.^[26–30] However, the existing hybrid designs for TENGs and EMGs generally utilize the identical driving devices to motivate both units in synchronous operation. The start-up wind speed and rotation speed (or frequency) of the two units are irrevocable regardless of changing environments, causing the hybrid wind energy harvesting devices to fail continuously and reliably supply the sensing terminals in the natural environment. Consequently, searching for an environmental self-adaptive hybrid technology with advantages of TENGs in low wind-speeds while maintaining a high energy conversion at strong winds, could be prospective to realize the wide-range and high efficiency wind energy harvesting.

Moreover, the practical performance of the environmental self-adaptive broadband wind energy harvesting system at the applicable terminals remains contingent on the power management electric circuit topology.^[31] Numerous energy management strategies for TENGs have been proposed recently, via transformers, DC buck conversions, or air discharge switches.^[32–34] Nonetheless, the existing electric circuit topologies of switching methods lack features that incorporate self-adaptability and single-board integrity. While the wind energy harvesting system switches between slow and fast wind conditions, the substantial variations in matching impedance and output characteristics between the TENG and the EMG could emerge, and thus the power management circuits should be mandated to operate in separate topologies.^[35–37] Meanwhile, the autonomous switching operation of the power management topology supposedly consumes minimal energy, rendering an incompatibility with existing stand-alone switching devices with notable switching losses. The inefficiency caused by poor integration of energy management will shorten the continuous operation time of the self-powered system, which in turn deteriorates the information

immediacy of IoT. Furthermore, the power management electric circuit topology design strategies with self-regulation features are inspiring for performance boost studies of any dual or multiple hybrid natural energy harvesting.

In this work, a self-powered system based on triboelectric-electromagnetic hybridized nanogenerator (TEHG) with a dual-channel power management topology (DcPMT) is proposed to achieve high efficiency and wide-range wind energy harvesting. The TEHG is designed as a cylindrical structure and two coaxial rotors are utilized for the TENG and EMG portions. For the purpose of overcoming the drawbacks of existing hybrid structures, the advantage of the proposed hybrid method relies on the concentric dual-axis rotational kinematic mode, which is the first reported structure in the field of wind energy harvesting that allows the EMG and the TENG to be operated at different wind speeds. By applying dual-rotation shift wind cups with calibrated arm lengths to motivate the rotators, the optimal aerodynamic characteristics enable the TENG and the EMG to, respectively, operate in their efficiency zones, facilitating the dual-stage even multi-stage energy harvesting. To enhance the output performance, the different hybrid forms of the TEHG were mathematically and experimentally compared. Based on the optimal design of the pole-pairs for the TENG and the EMG, the output power is enhanced and the total power curve becomes smooth. Moreover, the DcPMT is established and integrated on a printed circuit board (PCB) connecting with the TEHG to convert both the output from the TENG and EMG parts into a standardized DC supply for the commercial sensors. The proposed hierarchical topology design employs a combination of the isolated energy storage method and the undervoltage-lockout strategy for minimizing the static losses. On the basis of the above modifications, the environmental self-adaptive TEHG can effectively collect wind energy with a start-up wind speed dropping at 2 m s^{-1} , and the switching wind speed is $\approx 7\text{ m s}^{-1}$. The output power of the TEHG device increases with wind speeds and can reach a maximum value of 16.5 mW with a power density of 41.05 W m^{-3} , in which the TENG output power contribution is more than 70% at low wind speeds, and an energy conversion efficiency of 40–60% can be maintained. Furthermore, a self-powered system consists of the TEHG with the DcPMT and commercial environmental sensors were fabricated integrally to demonstrate the practicable feasibility. This batch-replicable hybrid structure of TEHGs and the single-board integrated DcPMT could potentially be installed in large-scale power grids and communication networks, which empowers the ubiquitous wind energy harvesting strategy over full speed regions, underpinning the future IoT infrastructure.

2. Results and Discussion

2.1. Structure and Working Principle of TEHG

As illustrated in **Figure 1a**, a wind-driven self-powered system with the capability of harvesting wind energy and driving the sensors to collect environmental information, contains a TEHG, a DcPMT, and an integrated commercial sensor chip. The real-time data collected by the proposed self-powered system can be

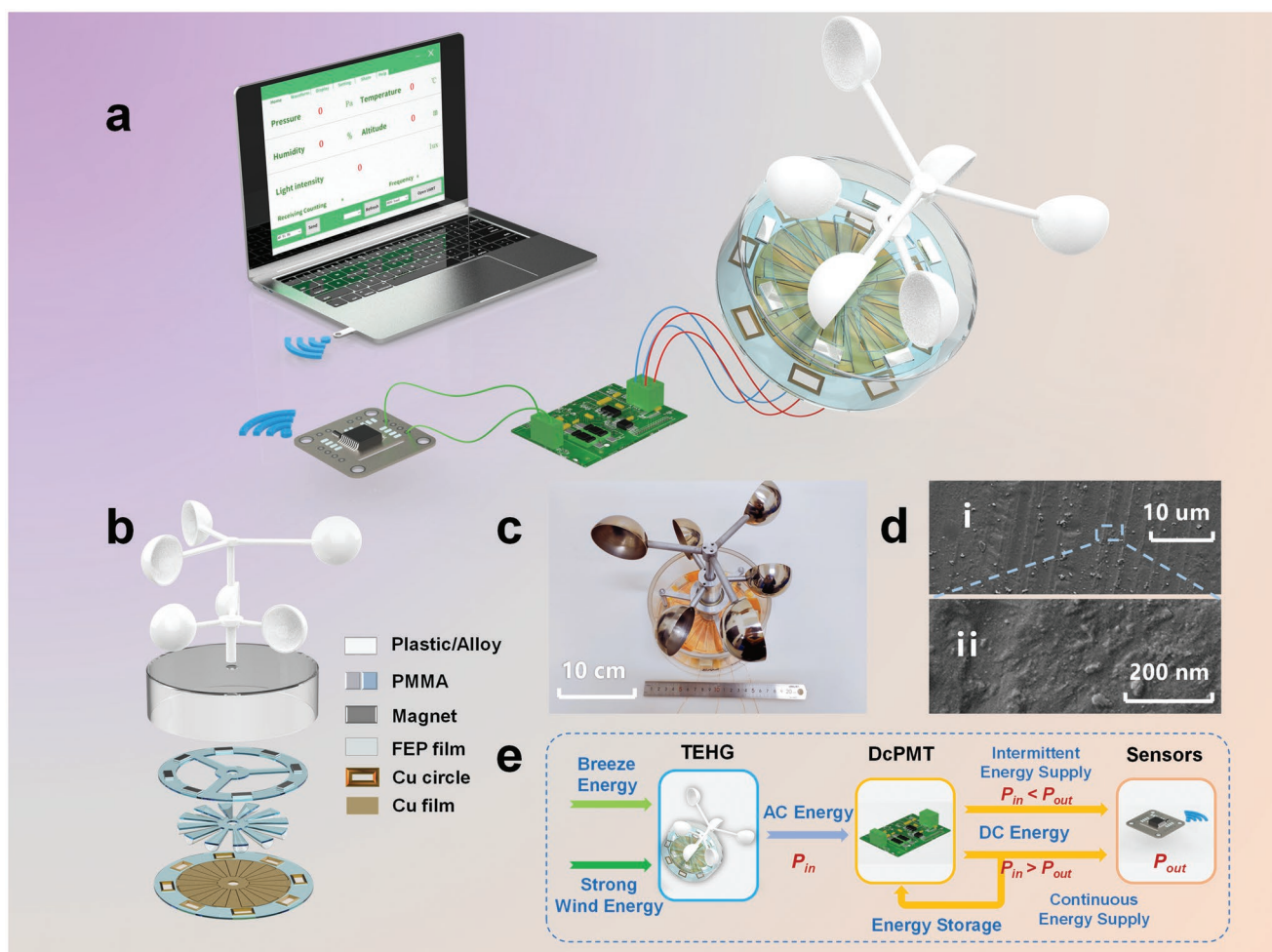


Figure 1. Structural design of TEHG and the wind-driven self-powered system. a) Schematic illustration of wind-driven self-powered system, which consists of a TEHG as the generator, a commercial sensor chip as the load, and a DcPMT to store and manage the energy. b) Expanded structural schematic of TEHG, which contains two coaxial dual rotating shaft wind cups as the wind energy collection module without the specific requirement for the orientation, and a drum-shaped packaged electro–mechanical transformation module constituted by the annular rotor with strong magnet blocks, the radial rotor with FEP files, and the bottom stator for both rotators. c) Platform photograph of TEHG. d) SEM images for FEP film (i) and its partial magnification (ii). e) Schematic illustration of the energy flow of the wind-driven self-powered system.

wirelessly transmitted to the data terminal equipment (e.g., the laptop in this paper). The detailed structural view of TEHG is schematically presented in Figure 1b. Concretely, the TEHG is a cylindrical structure that consists of two coaxial dual rotating shaft wind cups with different arm lengths as a wind energy collection module, and an electro–mechanical transformation module that is enclosed in a drum-shaped acrylic encapsulation. Herein, the wind cup with longer arm length is connected to a thin and solid rotating shaft, while the shorter one is fixed on another wide-aperture and hollow rotating shaft. By penetrating the solid shaft into the hollow one, the two coaxial wind cups are capable of independently operating. Inside the drum-shaped package is a multilayer hybrid unit that consists of two rotors and a stator (Figure S1, Supporting Information). The annular one is EMG rotor that consists of a circular acrylic plate with eight evenly distributed strong magnet blocks inlay and three spokes to connect the plate to the hollow rotating shaft. The lower surfaces of these embedded magnets are flush with the annular plate, and the adjacent magnets have opposite

polarity that produces an alternating magnetic field at the space below the rotor. Another radial rotor is the TENG rotor which consists of 12 fan-shaped units separated by equal central angle intervals, with a degree of 15° for each unit and interval. Specifically, each fan-shaped unit has a fluorinated ethylene propylene (FEP) film fixing on its two sides and covering the bottom space of the unit as a triboelectric surface. The film is also fan-shaped and appropriately larger than the unit, so that the middle part of the film could be naturally arched to contact with the stator. The two rotors share the one stator, which also serves as the bottom lid of the drum-shaped package. This disk-shaped stator could be divided into two parts. The inner one is a discoid area which belongs to the TENG part, while the outer is annular and belongs to the EMG. For the TENG part, the inner part could be totally covered by the vertical projection of the TENG rotor. On the upper surface of the discoid area, there is a set of graphically complementary Cu electrode sectors. The sectors are insulated by fine grooves, and each of the sectors is fitly equal to the single fan-shaped unit of TENG

rotor. Moreover, each adjacent sector has the opposite polarity thus belonging to different electrode groups. By connecting the adjacent sectors at one end with some spokes, the sectors of same polarity constitute a congregated electrode in parallel. For the EMG part, eight Cu coils are imbedded in the annular area equidistantly and symmetrically, so that the vertical projection of the strong magnet blocks on the EMG rotor could fully cover the center area of Cu coils. Furthermore, the vertical distance between the two rotors and the stator should be properly adjusted so that the FEP films of TENG are capable of contacting and completely covering a congregated electrode without touching the other. Meanwhile, the distance between the EMG rotor and the stator should be kept at around 1 mm to avoid collisions during high speed rotation.

As shown in Figure 1c, the device has dimensions of 24 cm × 24 cm × 20 cm (L × W × H), showing a favorable structural simplicity and portability. In addition, the polymers as the core of the TEHG are also easily accessible even for the potential mass production. The scanning electron microscope image (i) of the FEP film and its partial magnification image (ii) are shown in Figure 1d. The untreated FEP film has a smooth surface at a nanoscale with the arithmetic average roughness R_a of 6 nm, which was obtained from the NanoScope analysis software. While the TEHG is driven by wind energy and outputs AC energy that varies with wind speed, the outputs of both the TENG and EMG need to be managed, stored, and normalized by the DcPMT to drive the sensor. The schematic of the energy flow of this progress is shown in Figure 1e. First and foremost, by the collaboration between the two parts of TEHG, the wide-range natural wind energy is harvested and converted into AC electric energy to be stored in the DcPMT. Since that, the DcPMT will ponder the magnitude of winds and the energy it stores to decide the way it powers the sensors. For the situation of breeze as well as the energy storage not being sufficient, the DcPMT will enter the mode of intermittent energy supply, driving the sensor intermittently after each period of energy storage. Another situation is that when the wind is strong or the energy storage is sufficient, the DcPMT will enter into the continuous energy supply mode, generating a stable DC voltage output of 3.3 V at the output to drive the sensor operation. Meantime, the extra power will also be stored in the DcPMT to provide a compensation when wind speed drops.

The working principle of the hybrid nanogenerator includes two parts: the TENG part and the EMG part. Concretely, the operation of the TENG part is based on the combination of contact triboelectrification and electrostatic induction, while the EMG part is based on Faraday's electromagnetic induction effect. For the TENG part, Figure 2a illustrates the electricity generation process from the relative motion of FEP film and Cu electrode. We define the initial state as when the film completely covers an electrode (Figure 2a[i]), which is named electrode-A, and the adjacent electrode is the electrode-B. In the initial state, the FEP film is completely in contact with electrode-A, generating negative charges on the lower surface of the film through the triboelectrification. Correspondingly, equal positive charges in the loop will be attracted to the upper surface of electrode-A due to the electrostatic induction. As the FEP film moves from electrode A to electrode B, the electrostatic induction will drive the positive charges in the loop from electrode A to electrode B, generating a current flow via load from electrode A to electrode

B (Figure 2a[ii]). By the time when the FEP film is detached from electrode A and completely overlaps with the electrode B (Figure 2a[iii]), all the positive charges will be attracted to the upper surface of electrode B, which is regarded as the end of the first half cycle of electricity generation. Thereafter, the FEP film starts to move from electrode B to electrode A (Figure 2a[iv]), creating a reverse load current in the loop. Once the FEP film fully contacts with electrode-A again, a complete cycle of electricity generation by TENG is finished. In the condition of open-circuit, the charges cannot transfer between electrodes freely, thus the accumulated charges will create a periodic potential difference between the two electrodes by electrostatic induction shielding. For further understanding, Figure 2b visualizes the continuous variation of the open-circuit voltage (V_{oc}) of the TENG through finite-element simulation using COMSOL. The maximum amplitude of V_{oc} occurs when the FEP film completely covers one electrode without touching the other (Figure 2b[i,iii]). As the FEP film moves from one electrode to the other, the V_{oc} gradually decreases to zero and then increases in the opposite polarity. The trans-zero point occurs when the FEP is in the middle of the two electrodes (Figure 2b[ii,iv]), where the charges are equal on the two electrodes.

Figure 2c shows the 3D model established in COMSOL to illustrate the electricity generation process of the EMG part. The model contains eight rectangular Cu coils evenly distributed along a circumference with a radius of 75 mm and eight comparable sized strong magnet blocks which are placed above the coils with an interval of 1 mm. The dimensions of magnet blocks are 20 mm × 10 mm × 3 mm (Length × Width × Height), and each adjacent magnet has opposite polarity. Herein, we define the magnet with opposite polarity as magnet-A and magnet-B, respectively. As the EMG rotor revolved, the rotated magnets will create an alternating spatial magnetic field at the bottom of the rotator. This alternating spatial magnetic field will generate an electromotive force in the coils due to the Faraday's electromagnetic induction. The visualized continuous variation of voltage and magnetic field in the coils are demonstrated in Movies S1 and S2, Supporting Information, respectively. Moreover, the relative position of a coil to the magnet blocks is shown in Figure 2d. To more clearly visualize the relative motion of the magnet and the coil within one cycle, we have chosen to use the magnet as a reference to demonstrate the movement of the coil between the magnets. The variation in magnetic flux from the initial state (Figure 2d[i]) to the zero state (Figure 2d[ii]) will induce an electromotive force in the coil and drives the electric charges in the loop via the load. The maximum reverse magnetic flux linkage through the coil occurs when the coil overlaps with magnet-B (Figure 2d[iii]). As the rotator continues to revolve, the coil will move from magnet-B to magnet-A, leading to the reverse of magnetic flux. The generated electromotive force of the EMG part during one cycle is shown in Figure 2e, while the continuous variation of the magnetic flux as well as magnetic scalar potential is visualized through finite-element simulation, as shown in Figure 2f.

2.2. The Output and Characteristics of TEHG

To test the output performance of TEHG, a wind turbine system with adjustable wind speed controlled by applied voltage (Figure S2, Supporting Information) is used to simulate the

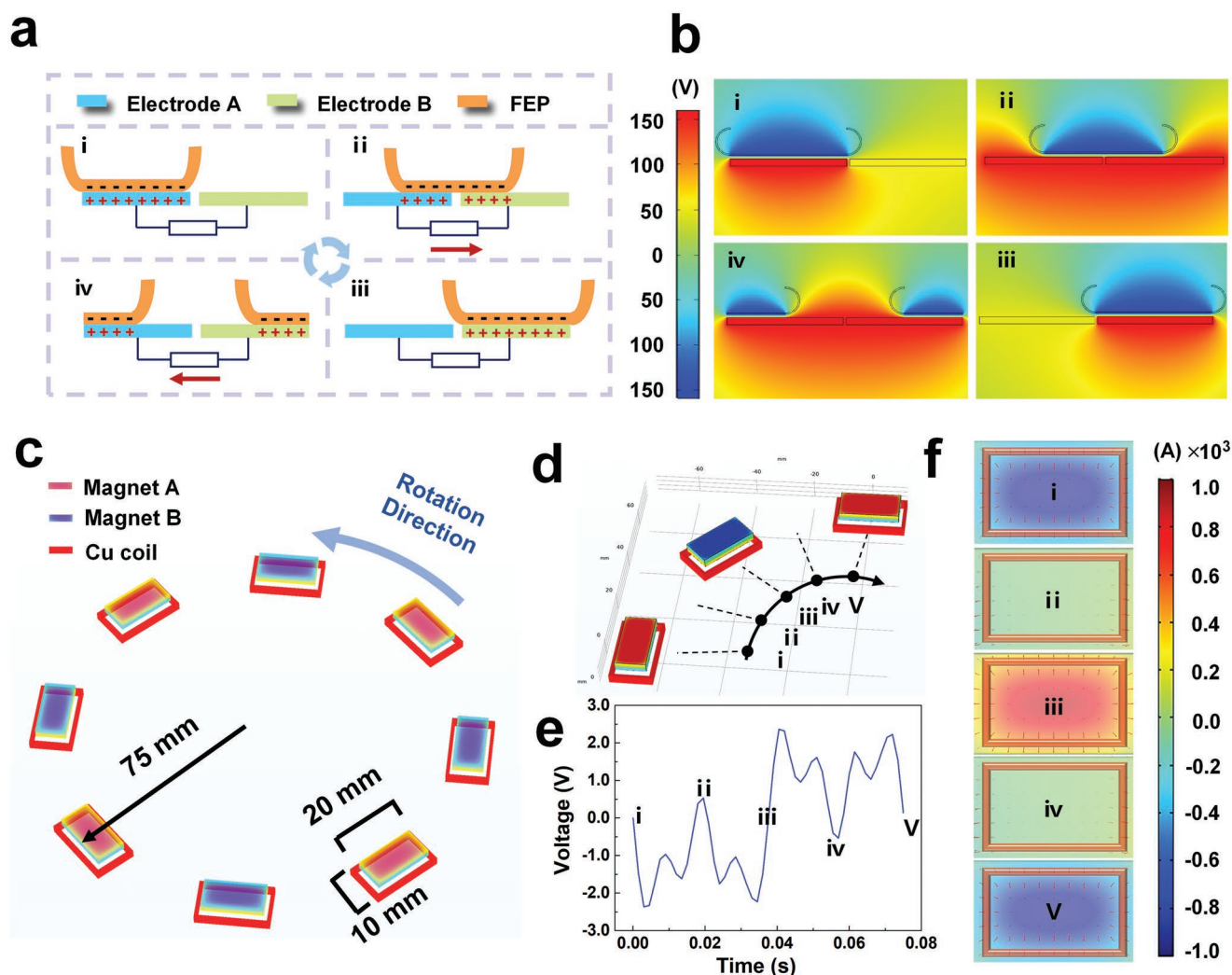


Figure 2. Schematics of working mechanism of TENG. a) Schematic illustrates the charge distribution and current direction of the TENG part in a whole cycle (i–iv) and b) electric potential distributions at corresponding displacements by COMSOL employing the finite-element method (i–iv). c) Schematic view of the EMG’s 3D model established in COMSOL and d) the relative position of a coil to the magnet blocks during the rotation. e) Calculated electromotive force of the EMG in a whole cycle (i–v) through the finite-element simulation using COMSOL and f) magnetic flux and magnetic scalar potential in coil at corresponding displacements.

wind energy with the wind speed range of $0\text{--}16.2\text{ m s}^{-1}$, and an infrared speed sensor is applied to measure the rotational speed of the TENG rotor and EMG rotor at different wind speeds. Subsequently, by using a CNC-regulated speed motor to precisely control the rotation speed of the two rotators, the open-circuit voltage (V_{oc}), short-circuit current (I_{sc}), and transferred charge quantity (Q_{sc}) of the TENG and EMG at different wind speeds could be accurately and steadily obtained. The output performance of this hybrid nanogenerator consists of two parts, which is the V_{oc} , I_{sc} , and Q_{sc} of the TENG (Figure 3a–c) and the V_{oc} and I_{sc} of the EMG (Figure 3d,e). For the TENG part, V_{oc} and Q_{sc} shows an uptrend in breeze with wind speed range of $2\text{--}5.4\text{ m s}^{-1}$ then remain almost constant value of 300 V and 120 nC, while I_{sc} exhibit a positively proportional relationship with wind speed during the whole range, with the initial value of $2\text{ }\mu\text{A}$ to the maximum value of $30\text{ }\mu\text{A}$. The reason why V_{oc} and Q_{sc} of the TENG remain essentially constant in the stable

operation is the working principle of freestanding mode of soft-friction TENG. The mechanism analysis of the TENG module is detailed in the Equations S1–S5, Supporting Information.

For the EMG part, the V_{oc} and I_{sc} denote the same trend with wind speed as shown in Figure 3d,e. It can be seen that the operation of EMG needs a start-up wind speed around 4 m s^{-1} . The V_{oc} and I_{sc} of EMG exhibit a positively proportional relationship with wind speed from $4\text{ to }16.2\text{ m s}^{-1}$, with the initial values of 0.23 V and 0.34 mA to the maximum value of 4.4 V and 8.7 mA, respectively. This linear relationship is consistent with the Faraday’s law, in which the electromotive force (V_{oc}) induced in a coil is proportional to time-rate variation of magnetic flux linkage through a coil. Therefore, the induced V_{oc} in a coil is expressed as Equation (1).

$$V_{oc} = -N \frac{d\Phi}{dt} \quad (1)$$

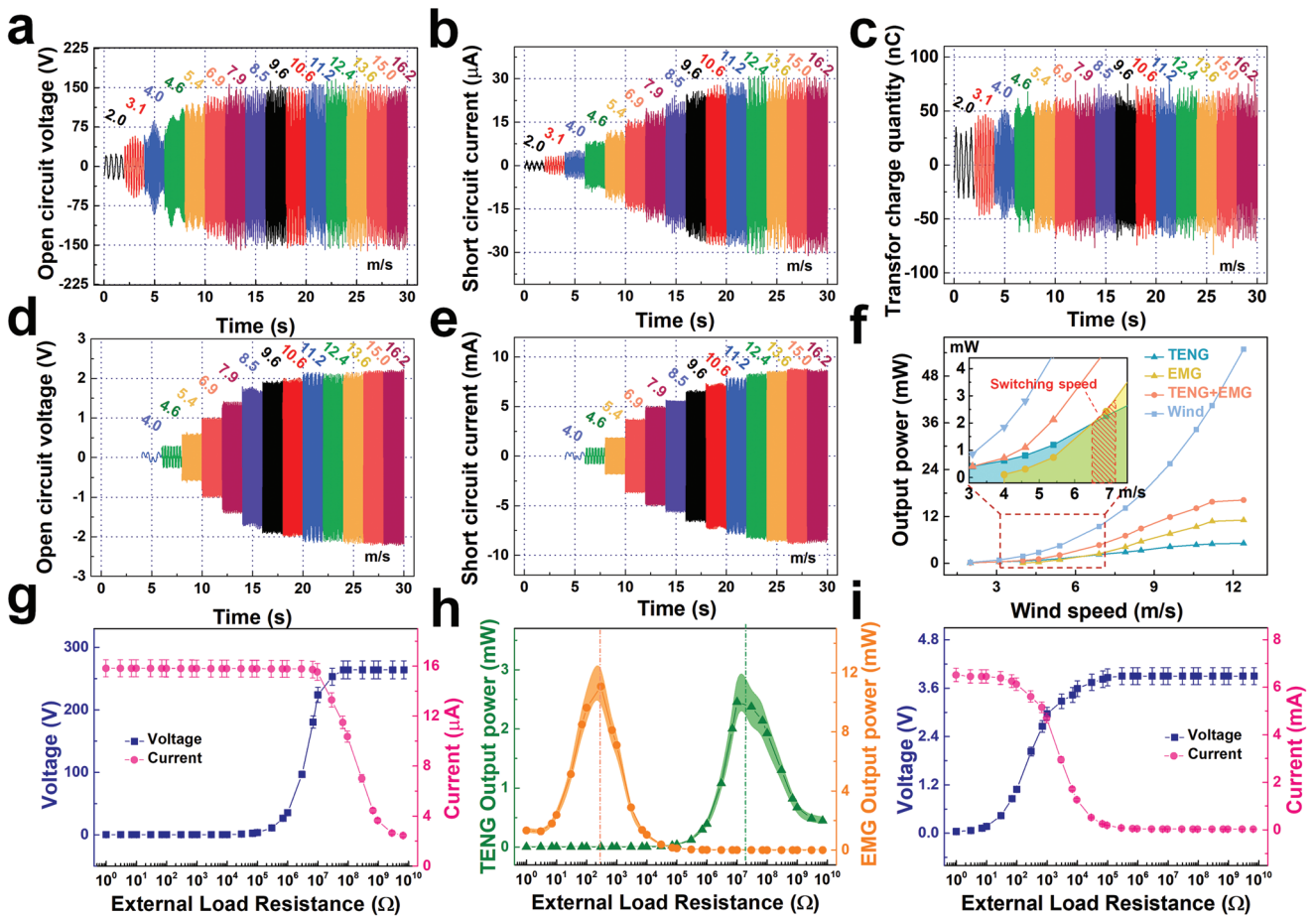


Figure 3. Electrical measurements of the TEHG. a) V_{oc} , b) I_{sc} , and c) Q_{sc} of the TENG under typical wind speeds. d) V_{oc} and e) I_{sc} of the EMG under typical wind speeds. f) Output power of TENG, EMG, and the sum of both at different wind speeds compared with the wind energy passing through the device, in which the load resistance of TENG is 10 M Ω and that of EMG is 300 Ω . Amplitudes of output voltage and current of the g) TENG and i) EMG under varied external load resistance, which are tested at the switching wind speed of 6.9 m s⁻¹ for TENG and the saturation wind speed of 10.6 m s⁻¹ for EMG. h) Dependences of output peak power on varied resistive loads for TENG at 6.9 m s⁻¹ and EMG at 10.6 m s⁻¹.

where Φ is the total magnetic flux linkage in each turn of the coil and N is the number of turns of the coil. Assuming that the magnetic field generated by a rectangular magnet is uniformly distributed in the rectangular local spatial below the magnet, then the induced electromotive force in the coil can be estimated as Equation (2).

$$\frac{d\Phi}{dt} = B \frac{dS(\theta)}{d\theta} \frac{d\theta}{dt} = \frac{B}{120\pi} \frac{dS(\theta)}{d\theta} n \quad (2)$$

where B is the magnetic flux density in the rectangular space below the magnet, $S(\theta)$ is the overlapping area of the uniform magnetic field with the coil, and θ is the radian of rotor rotation. According to Ohm's law, the I_{sc} of EMG can be expressed as Equation (3).

$$I_{sc} = \frac{V_{oc}}{R_{coil}} = - \frac{NB}{120\pi R_{coil}} \frac{dS(\theta)}{d\theta} n \quad (3)$$

where R_{coil} is the internal resistance of the coil. According to Equations (2) and (3), both V_{oc} and I_{sc} of EMG are linearly

dependent on the rotational speed. As a result, when the EMG is operated at the wind speed above the start-up wind speed, the V_{oc} and I_{sc} will be enhanced as the wind speed increases from 4 to 16.2 m s⁻¹.

The complementary wind energy harvesting of the two components of TEHG can be seen from their output power curves. Here, Figure 3f shows the output power of TENG, EMG, and the sum of both at different wind speeds, in which the load resistance of TENG is 10 M Ω and that of EMG is 300 Ω . The detailed contribution ratios of the TENG and EMG are shown in Figure S3, Supporting Information. In the low speed range (2–5 m s⁻¹), the TENG can provide an output power from 0.12 to 1.2 mW which significantly exceeds that of the EMG in same wind speed range, making TENG the major power contributor of the hybrid nanogenerator in breeze, where the EMG output power contribution is less than 30% based on our testing results in Figure 3f and Figure S3, Supporting Information. As the wind speed continues to rise, the output power of the TENG keeps rising with a maximum value of 5.2 mW, but the growth rate is inferior to that of the EMG. For the EMG, the output power appears in the range wind speed above 4 m s⁻¹, and the

power will rapidly rise and exceeds that of the TENG at the wind speed of 6.5–72 m s⁻¹ (switching speed area in the inset of Figure 3f). The switching wind speed is affected by three main factors, including the size of the wind cup, the arm length of the wind cup, and the mechanical–electrical load, where the load is not only the external electrical load in the narrow sense, but also the frictional resistance inside the rotating shaft. Once the transcendence is finished, the primary power contributor of the device will switch from TENG to EMG. As the wind speed continues to be magnified, the output power of EMG will keep increasing, until the wind speed exceeds 10.6 m s⁻¹, the growth rate gradually slows down, and the output power finally keeps at the maximum value of 12 mW. The output power of the TEHG is calculated as the sum of the two components. Assuming that the wind blows vertically through the energy capturing device from the horizontal plane, the wind power P_{wind} through the cross section is

$$P_{\text{wind}} = 0.5 \times S \rho v_{\text{wind}}^3 \quad (4)$$

where S is the effective cross-sectional area blown by the wind, which is calculated as 0.048 m² for this wind energy harvesting device. ρ is the density of air, which is estimated as 1.2 kg m⁻³. The v_{wind} is the wind speed from 0–16.2 m s⁻¹. As shown in the inset of Figure 3f, although the power curves of both TENG and EMG have large variability with the power of the wind (i.e., insufficient output in strong wind or incapable operation in low wind speed), the total output power of the hybrid nanogenerator aligns well with the power curve of wind energy before the wind speed rises to 12 m s⁻¹, demonstrating a characteristic of wide-range and efficient wind energy harvesting of the TEHG.

Figure 3g–i shows the amplitudes of output voltage, current, and power under varied external load resistance of the TENG at the switching wind speed of 6.9 m s⁻¹ and the EMG at the saturation wind speed of 10.6 m s⁻¹. Here, we take the TENG, for example, as the load impedance increases, the amplitude of the output current drops while that of output voltage appears a reverse trend. The instantaneous output power shows a trend of increasing followed by decreasing, corresponding to a maximal output power of 2.5 mW at the load resistance of 10 M Ω . The trends of the EMG are similar with TENG, and the maximal output power of EMG is estimated as 11 mW while the matching impedance is 300 Ω .

2.3. Structural Optimization

2.3.1. Optimization of Aerodynamic Performance

To explore the aerodynamic performance, three wind cups with diameters of 5, 6, and 7 cm, and five replaceable arms with different rotating radii from 5 to 9 cm with an interval of 1 cm were custom-manufactured as shown in the schematic diagram in Figure 4a and the photograph in Figure S4, Supporting Information. Figure 4b plots the inverse linear relationship between the start-up wind speed and saturation rotation speed as the arm length increases. By comparison, owning a smaller start-up wind speed of 2.9 m s⁻¹, the wind cup with radius of

6 cm can be combined with the 9 cm radius wind cup, which belongs to the efficient interval of the EMG part. Therefore, the arm lengths of the dual rotating shaft wind cups are selected as 9 and 6 cm, respectively. The process for the optimal parameters calibration from the detailed comparative analysis can be found in Figure S5a, Supporting Information. Furthermore, the diameters of the two wind cups are selected in different sizes to analyze the influence of aerodynamic performance as shown in Figure 4c. The start-up wind speed of wind cups shows an inverse proportional relationship with the diameter, while the saturation rotation speed shows an uptrend followed by a downtrend as the diameter increases. The wind cup with the diameter of 6 cm has the highest saturation rotation speed of 480 rpm, which is much higher than the other two.

The reason for the variation of the start-up wind speed and saturation rotation speed with different arm lengths and diameters is attributed to the torques. For any fixed-size wind cup, the driving force (F_{wind}) is proportional to the windward area of the wind cup (S_{cup}) and the square of the velocity difference between wind and the cup (Δv), as shown in Equation (5).

$$F_{\text{wind}} = k S_{\text{cup}} \Delta v^2 = k S_{\text{cup}} (v_{\text{wind}} - v_{\text{cup}})^2 \quad (5)$$

where k is the proportionality factor (kg m⁻³), S_{cup} is the windward area of the wind cup, v_{wind} is speed of the wind blowing through the wind cup in horizontal direction, and v_{cup} is the linear velocity of the wind cup, which can be calculated by the rotational speed n (r min⁻¹) as

$$v_{\text{cup}} = \frac{\pi R}{30} n \quad (6)$$

where R is the arm length of the wind cup, as illustrated in Figure 4a. Thus, the wind cup can provide a torque as below.

$$T = F_{\text{wind}} R = k S_{\text{cup}} \Delta v^2 R \quad (7)$$

Once the device starts to rotate, the inducement of the torque will change into sliding friction with the torque of T_f . As the wind speed increases, the wind will compress the rotator to create more frictional resistance, resulting in an addition of the resistance torque as T_Δ . Besides, the electromechanical conversion of the TEHG also requires a torque as T_e . In stable operation, the driving torque will overcome the resistance torques above and form a balance, which can be expressed as Equation (8). Then the rotation speed (n) can be calculated from Equations (5–7) as Equation (9).

$$T = T_e + T_f + T_\Delta \quad (8)$$

$$n = \frac{30 v_{\text{wind}}}{\pi} \left(\frac{1}{R} \right) - \frac{30}{\pi} \sqrt{\frac{T_e + T_\Delta}{k S_{\text{cup}}}} \left(\frac{1}{R} \right)^{-1.5} \quad (9)$$

It can be seen that the rotation speed n consists of a linear part and a nonlinear part with the inverse of arm length ($1/R$). The curves of n versus $1/R$ at low wind speed of 4–5 m s⁻¹ and high wind speed of 9–16 m s⁻¹ were experimentally tested to show the above variation process, as shown in Figure S5b,

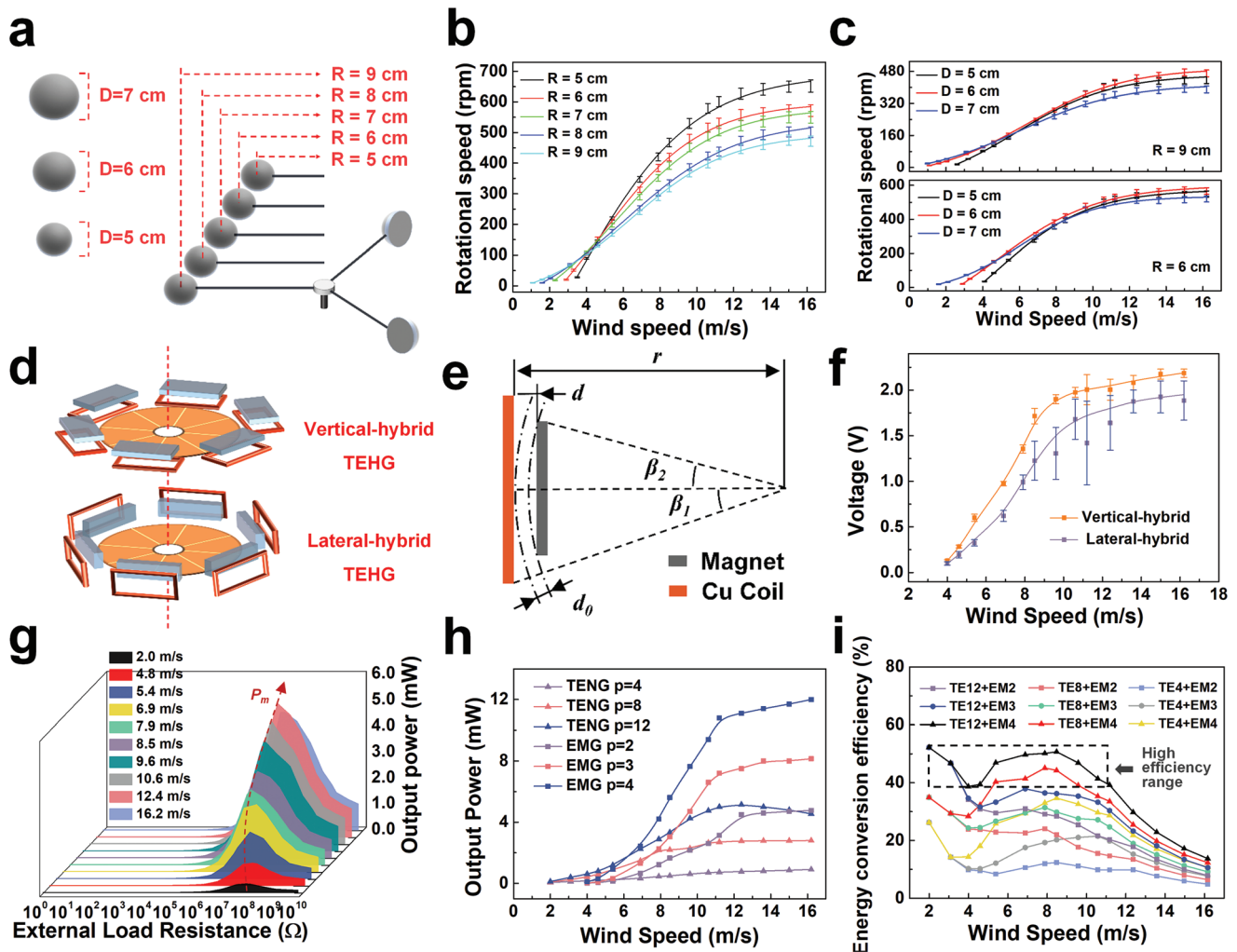


Figure 4. Structural parameters optimization of TEHG. a) Schematic diagram of aerodynamic tests for wind cups with different arm lengths. b) Schematic diagram of relationships between the saturated rotation rates versus the start-up wind speed for the different arm lengths. c) Measured relationship between the rotational speed and wind speed of wind cups with varied arm lengths. d) Schematic diagram of the vertical-hybrid TEHG and the lateral-hybrid TEHG. e) Schematic diagram of magnetic flux density calculation for lateral-hybrid TEHG. f) The voltage versus wind speed obtained by measurement for the vertical-hybrid TEHG and the lateral-hybrid TEHG. g) Output power variation curves of TENG with its $p = 12$ tested with a series of different load impedances. h) Comparison of the output power varies with wind speed for TENGs and EMGs with different p -values. i) Variation of the energy conversion efficiency of TEHG with wind speed for different p pairings.

Supporting Information. In addition, it follows from Equation (9) that a larger D , that is, a larger S_{cup} , yields a larger n . Meanwhile, as D continues to increase, the mass of wind cup becomes non-negligible and the wind cup requires a large driving torque in its rotation to balance the additional growth of T_{Δ} .

Based on the above experimental results and comparative analysis, a wind cup with 9 cm R and 6 cm D was chosen to be paired with another wind cup with 6 cm R and 6 cm D , which achieves a no-load aerodynamic characteristic of start-up wind speed at 1 m s^{-1} . Once TENG and EMG are loaded, the aerodynamic performance curves were measured and are observed to shift to the right, while the starting and switching wind speeds grow to 2 and $\approx 7 \text{ m s}^{-1}$, respectively, which indicates the validity of the optimization for the aerodynamic performance as shown in Figure S5a and Movie S3, Supporting Information.

2.3.2. Optimization of Hybridization Forms

The hybridization form is an important influencing factor on the electrical output performance of the TEHG. Therefore, Figure 4d–f displays the optimization of hybridization forms. Here, a vertical-hybrid TEHG is designed to be compared with a lateral-hybrid TEHG to investigate the effect of the hybrid form on the output performance, as shown in Figure 4d. For the vertical-hybrid TEHG, the magnets and coils are fixed horizontally in the outer annulus of the circular rotor disk and stator, with the vertical projection of the magnet falling just in the center of the coil, completely covering the rectangular cavity of the coil. Distinctively, the EMG portion of the lateral-hybrid TEHG has a cylindrical rotor, and the magnet blocks are set uniformly on the side walls of the cylindrical rotor in a vertical position.

For the TENG part, an important goal is to provide the highest possible output current. In our previous work, the effect of disk TENG size on output current was discussed, showing a linear growth relationship between current and TENG area. For the EMG part, the weak voltage is an important limiting factor in small wind energy harvesting. According to Equation (2), structural optimization is needed to make the $d\Phi/dt$ larger to boost output voltage. Ideally, the magnet blocks should be placed as close as possible to the coils to obtain a larger flux density. Furthermore, the flux density can be approximated by a point at a distance d from the magnet center as in Equation (10) (as the schematic diagram in Figure S6, Supporting Information).

$$B = \frac{B_r}{\pi} \left[a \tan \left(\frac{ab}{2d\sqrt{a^2+b^2+4d^2}} \right) - a \tan \left(\frac{ab}{2(d+h)\sqrt{a^2+b^2+4(d+h)^2}} \right) \right] \quad (10)$$

where B_r is the remanence of magnet blocks (1–1.2 T for NdFeB magnets), a , b , and h are the length, width, and thickness of the magnet block, which are equal to 20, 10, and 3 mm, respectively.

For the vertical-hybrid TEHG, the d is equal to 1 mm, so the B of vertical-hybrid TEHG can be calculated by Equation (10) as 0.19 T. By studying the magnets passing over the upper surface of coils during rotation (Figure S6a,b, Supporting Information), the magnets and coils coincidence area (S) of the vertical-hybrid TEHG is a function of the rotation angle (θ). The function of S and θ consists of two parts can be obtained as below.

$$S_1 = ab - 2br \tan \frac{\theta}{2} - \left[\frac{a}{2} - \left(r + \frac{b}{2} \right) \tan \frac{\theta}{2} \right]^2 \tan \theta, \theta \in \left[0, 2a \tan \frac{a}{2r+b} \right] \quad (11)$$

$$S_2 = a \left(\frac{b}{2} - r \right) + \left(\frac{b}{2} - r \right)^2 \tan \frac{\theta}{2} + \frac{a^2}{4 \tan \frac{\theta}{2}}, \theta \in \left[2a \tan \frac{a}{2r+b}, 2a \tan \frac{a}{2r-b} \right] \quad (12)$$

where r is the distance from the center of the coil to the axis of rotation, which is 68 mm. Therefore, the induced electromotive force waveform in each coil of the vertical-hybrid TEHG can be calculated by Equations (2) and (10–12). Further, the V_{oc} waveform of the EMG at a wind speed of 10 m s⁻¹ is calculated (Figure S6f, Supporting Information), which is a square wave-like AC waveform possessing a maximum voltage of 2 V. Moreover, the V_{oc} waveform simulated by COMSOL and obtained from experiments are also displayed (Figure S6g, Supporting Information) as a corroboration.

For the lateral-hybrid TEHG, both B and S are calculated differently than for the vertical-hybrid TEHG. Figure 4e shows the calculation of d for the lateral-hybrid TEHG, as shown in Equation (13).

$$d = r - (r - d_0) \cdot \cos \left(a \sin \frac{a/2}{r} \right) \quad (13)$$

where r is the distance of the coil center from the rotating shaft (70 mm), and d_0 is set to 1 mm. Then, the B of the lateral-hybrid TEHG is calculated as 0.17 T by Equation (10), which is smaller

than that of the vertical-hybrid TEHG. Here, S' represents the projected area of the cross section of the magnetic field across the coil as shown schematically in Figure S6c,d, Supporting Information, and can be expressed as below.

$$S' = \left(\frac{a}{2} - \sqrt{r^2 + a^2/4} \cdot \sin \left(\theta - a \tan \frac{a}{2r} \right) \right) \cdot b \quad (14)$$

Similarly, the V_{oc} waveform of the EMG in lateral-hybrid TEHG can be calculated by Equation (2) as shown in Figure S6f, Supporting Information. Compared with the vertical-hybrid TEHG, the V_{oc} waveform of the lateral one is closer to the square wave, but the V_{oc} amplitude is smaller.

Moreover, a lateral-hybrid TEHG was prepared to compare with the vertical-hybrid TEHG (Figure S7, Supporting Information). Figure 4f shows the voltage versus wind speed obtained by measurement for the vertical-hybrid TEHG and the lateral-hybrid TEHG. As the wind speed increases, the vertical-hybrid one can reach a maximum V_{oc} of 2.3 V, while the maximum V_{oc} of the lateral-hybrid one is only 1.8 V. In addition, the output voltage of the vertical-hybrid TEHG appears to be more stable compared to the lateral-hybrid TEHG. Therefore, considering the EMG as the main contributor to the hybrid generator at high wind speeds, the vertical-hybrid TEHG was finally chosen to ensure a strong and stable voltage output could be achieved under strong winds.

2.3.3. Optimization of TEHG Pole-Pairs

In the design of hybrid generators, both TENG and EMG can obtain greater power output by increasing their pole pairs. Herein, p represents the number of alternating current signals that will output at the generator electrodes for each rotation, and it also represents the number of sector cells of the rotor for the TENG. Meanwhile, p means the number of magnet pairs for the EMG rotator. For disk-like TENGs with fixed size, the I_{sc} increases linearly with p as illustrated Equation S5, Supporting Information, which means that a larger p can improve the charge transfer rate. The same optimization applies to the EMG due to the coils being connected in series and the induced voltages in the coils being synchronized. However, the additional p of EMGs requires the installation of more magnets and coils, thus making the mechanics of the EMG rotor weak and the mass of the device bulky. Collectively, the optimization of the pole pair value p should strike a balance between the output performance and the device weight.

Therefore, as shown in Figure S8, Supporting Information, three TENGs with p of 4, 8, and 12, and three EMGs with p of 2, 3, and 4 were fabricated and analyzed. The output power of TENG and EMG with different p values at different wind speeds and a series of load impedances were attained to figure out the matching impedance (R_m) and maximum output power (P_m), as displayed in Figure S9, Supporting Information. Taking the TENG with $p = 12$ as an example (Figure 4g), the R_m gradually decreases and basically stabilizes around 10 M Ω after the wind speed exceeds 7.9 m s⁻¹, while the P_m grows and finally stabilizes at a maximum value of about 5 mW. Compared with the TENG, the R_m of EMG remains $\approx 300 \Omega$ regardless of wind

speed, while its P_m increases with wind speed and reach 12 mW with the wind speed at 10 m s⁻¹. Furthermore, Figure 4h shows the power curves for each TENG at 10 MΩ load and each EMG at 300 Ω load for different wind speeds. Notably, the TENG can be started at about 2 m s⁻¹ and its output power increases basically linearly with the wind speed at low wind speed. On the other hand, the start of EMG occurs when wind speed exceeds 4 m s⁻¹, then the EMG output power rises rapidly and overtakes the TENG around 6 m s⁻¹. The saturation of the EMG output power occurs at the wind speed around 11 m s⁻¹. Figure S10a, Supporting Information, indicates the output power as a superposition of the two components. An excellent power curve requires smooth power growth as well as strong power output, which can be adjusted by the p -values of the TENG and the EMG. Figure S10b, Supporting Information, plots the efficiency curves of the TENG and the EMG, which are calculated by Equation (15).

$$\eta = \frac{P}{P_{\text{wind}}} \cdot 100\% \quad (15)$$

In this work, the TENG achieves a maximum energy conversion efficiency of 52% in the breeze, and the efficiency of the TENG decays continuously with the growing wind speed. Meanwhile, the EMG can only collect wind energy efficiently at stronger wind speeds, corresponding to a maximum efficiency of 30% at a wind speed of 8.5 m s⁻¹. Once the wind speed exceeds the switching wind speed, the instantaneous energy conversion efficiency of EMG will exceed that of TENG. Figure 4i shows the total energy conversion efficiency (η) of TEHG. The optimization target is set to the highest efficiency curve covering the full wind speed interval from 2 to 16 m s⁻¹. Therefore, an optimal p pairing (TENG 12 + EMG 4) was chosen to achieve an efficient (40–50%) and smooth power output with a maximum output power of 16.5 mW with a power density of 41.05 W m⁻³ over a wide wind speed range of 2–11 m s⁻¹.

2.4. Working Mechanism and Characteristics of DcPMT

Considering the difference in voltage amplitude and operating range between the TENG and EMG outputs of the hybrid generator, these two outputs cannot be simply connected in series or parallel to power the load. Here, a DcPMT for the TEHG is designed to manage the two electrical sources of the TEHG for common storage, management, and standardized DC voltage output. As shown in Figure 5a, the DcPMT consists of an energy collection-storage module and an energy management module. In the energy collection and storage module (Figure 5a[i]), the output voltage of TENG is converted to DC by a bridge rectifier and then charged to C_{store} by a diode. Compared to the traditional diode rectification methods, the EMG output power flows through an additional low-frequency step-up by a surface mounted boost transformer T before the rectification using low power Schottky diode (the forward voltage of ≈0.2 V), considering that the output voltage of EMG is low under the breeze range. The reason for using low-frequency transformer is the weak output voltage of EMG, especially in low wind speed of 4.0–6.9 m s⁻¹, where the V_{oc} of EMG is less

than 1 V, making it difficult to meet the voltage requirements of subsequent energy management circuits. In addition, there are differences in the voltage amplitudes of TENG and EMG at different wind speeds, so two diodes are used to limit the current flow and take part of the reverse voltage to protect the rectifier. On a related note, according to the testing results in Figure 4, the EMG output power contribution is less than 30% at low wind speeds, hence the overall TEHG output range characteristics are accommodated in the electronic component selection.

Following the conversion of electrical energy from the TENG and EMG modules to the charge in C_{store} using the above isolated synchronous storage topology, the DC output still needs to be calibrated to the 3.3 V nominal voltage for the commercial sensors. Consequently, an appropriate DC–DC conversion strategy plays a decisive role. Although the discrete electronic switching devices can be controlled to achieve a DC–DC conversion, the high switching losses and large static currents will dissipate the energy that has been meticulously collected from the wind, resulting in poor output efficiency. Therefore, a hysteresis voltage control method is implemented in this paper to reduce the switching losses and an undervoltage-lockout strategy is introduced to enhance the continuous stability of the output voltage, especially in the case for sensors as light loads. Compared to the single-limit comparison schemes, for example, the LTC3459 with a quiescent current ≈10 μA, the hysteresis DC–DC strategy configured with positive feedback control can reduce the quiescent current to the nA level, thus significantly suppressing switching losses. Specifically, considering that the quiescent current of LTC3588-1 chip is only 450 nA and the external topology can support undervoltage-lockout strategy, this paper develops the overall topology based on the integrated module of LTC3588-1 to compensate for the hysteresis voltage control, enabling a DcPMT design with minimized switching losses.

Figure 5a[ii] shows the energy management module based on a LTC3588-1 (Linear Technology) to manage the electrical energy stored in the C_{store} and provide standardized typical voltage outputs. The LTC3588-1 chip is a micropower low-loss buck commonly used in piezoelectric or triboelectric nanogenerators. The chip provides four typical voltage outputs of 1.8, 2.5, 3.3, and 3.6 V, which are selected and controlled via pins D_1 and D_2 . Here we take 3.3 V as an example to show the composition and schematic of the energy management module. The capacitors C_1 and C_2 are used to provide functional low and high potentials, and inductor L_1 is used to connect V_{out} pin to SW pin for feedback signals in the hysteresis voltage control process. C_{out} is the output capacitor of the circuit and also acts as a filter. Finally, the PCB shown in Figure 5b can be fabricated according to the above schematic. For the follow-up practical applications, the external package design of the DcPMT would further introduce insulation, anti-vibration, and dust-proof features. The enclosure could be designed with a high permeability shielding material in a hemispherical shape to avoid corona discharge damage.

After connecting the TEHG and load sensors to the ends of DcPMT, the wind energy can be collected, converted, and supplied to application. For the start of DcPMT, the terminal voltage of C_{store} needs to be charged to 5 V. Figure 5c shows the voltage curves of TENG and EMG in the energy harvesting

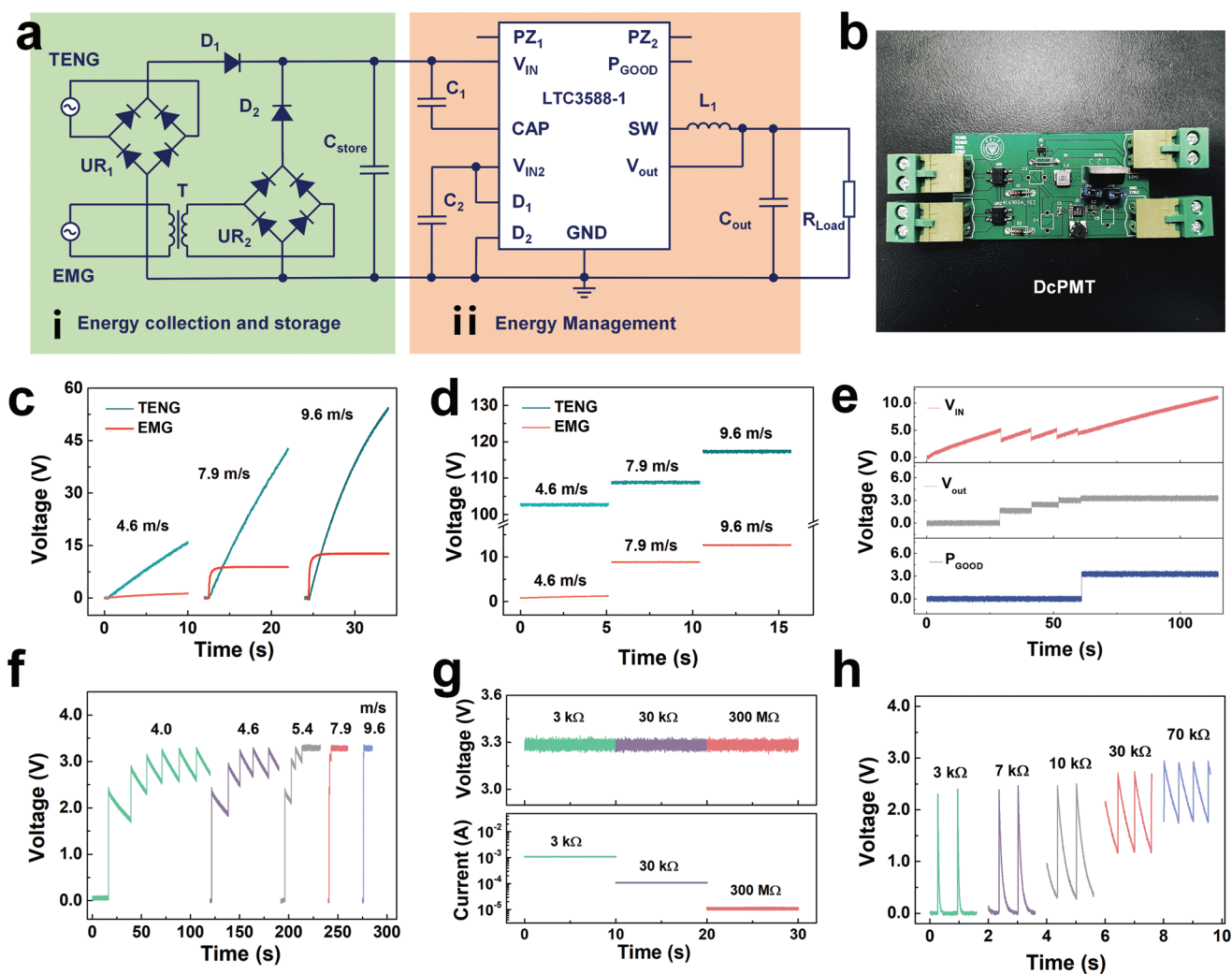


Figure 5. Schematic diagram of the DcPMT and its performance test. a) Schematic diagram and b) photograph of DcPMT. c) Capacitor charging curves and d) maximum capacitor charging voltages of TENG and EMG at different wind speeds. e) Start-up and operating principle test diagram of DcPMT. f) DcPMT start-up process at different wind speeds. g) Output voltage and current waveforms of DcPMT when wind resource or energy storage is sufficient and h) output voltage waveforms of DcPMT in intermittent supply mode when wind resource is scarce and energy storage is depleted.

and storage module of DcPMT for charging a $1 \mu\text{F}$ capacitor at different wind speeds, respectively. The charging voltage on the $1 \mu\text{F}$ capacitor is oriented toward the case of an off-load condition, which is intended to avoid the effects of the external load on the front charging section. It can be seen that the charging curve of TENG is basically linear, and the charging rate increases faster with higher wind speed. In contrast, the charging rate of EMG is faster, but the voltage is prone to saturation. Specifically, at 4 m s^{-1} wind speed, the EMG can charge the capacitor up to 1 V, which cannot reach the start-up requirement of LTC3588-1, while the TENG can easily reach a capacitor voltage of 15 V or more to drive the DcPMT. As the wind speed grows, the saturation voltage of EMG gradually increases, and the fast charging rate of EMG becomes more obvious. When the wind speed increases to 6.9 m s^{-1} , the saturation voltage of EMG increases to 8 V, and its charging rate before saturation is larger than that of TENG. This trend is more obvious when the wind speed increases to 9.6 m s^{-1} , and the saturation voltage

of EMG increases to 12 V, so that C_{store} can be charged to the operating voltage faster. It is worth noting that the TENG and EMG in operation are connected in parallel via diodes to charge C_{store} within an uninterrupted and non-interfering manner. Figure 5d shows the maximum capacitor charging voltage that can be achieved by TENG and EMG at different wind speeds, where the saturated charging time for the EMG and the TENG are 2.5 s and 8.6 min, respectively, as an example with a 7.9 m s^{-1} wind speed. It can be seen that the voltage of TENG can be basically stabilized above 100 V at different wind speeds, so that it can still charge the capacitor to the working voltage in light wind. The voltage of EMG is more obviously affected by wind speed, and it is difficult to realize effective utilization at low wind speed. As the wind speed increases, the voltage no longer becomes the limitation of EMG power supply, and its advantage of fast charging speed is given full play at this time.

In the operation of the energy management module, the voltage of C_{store} enters the LTC3588-1 chip from the V_{IN} and

output from V_{out} pin, while P_{GOOD} is used to give the logic signal to determine the output status of the DcPMT. Figure 5e shows the waveforms and relationships of V_{IN} , V_{out} , and P_{GOOD} during the output preparation of DcPMT at 6 m s^{-1} wind speed. The process can be divided into three stages. The first stage is the capacitor charging stage, where V_{IN} is charged to 5 V by TEHG around 30 s. During this process, V_{out} and P_{GOOD} are kept at 0 V and the DcPMT does not output externally. When V_{IN} reaches 5 V, the LTC3588-1 chip starts to boot and enters the second stage, the preparatory stage of power supply. During this phase, V_{IN} oscillates in a sawtooth pattern between 4 and 5 V, while V_{out} is charged in stages and rises in steps. After about 30 s, V_{out} is charged to 3.3 V. At the end of the preparation phase, the P_{GOOD} will generate a high signal, indicating that the DcPMT is ready and can enter the power supply phase. At this point, V_{IN} is unlocked and the excess energy collected by TEHG will keep V_{IN} rising and stored in C_{store} . After the load is connected, the power in C_{store} will be supplied to the load as 3.3 V DC, thus standardizing the output voltage. Figure 5f shows the V_{out} waveform of DcPMT during charging at different wind speeds. At this time, the P_{GOOD} output is 0 V, thus the charging process is carried out under no load. It can be seen that at a low wind speed of 4 m s^{-1} , it takes about 100 s for V_{out} to be charged to 3.3 V. As the wind speed increases, the charging time of V_{out} gradually decreases. When the wind speed is 9.6 m s^{-1} , the charging process of DcPMT takes only 2 s to be completed. Normally, DcPMT will store the excess energy to compensate for the weaker wind scenario when the wind is strong. When the wind is strong or the energy storage is abundant, DcPMT can continuously output 3.3 V DC voltage. In this case, the output voltage and current waveforms of DcPMT varies with a series of load resistance as shown in Figure 5g. The test was conducted at 9.6 m s^{-1} wind speed, and it can be seen that the voltage and current waveforms are very stable, demonstrating excellent power supply quality. The reason why DcPMT can create stable voltage outputs is based on the selected ultra-low quiescent current undervoltage-lockout strategy. By devising the external circuit, we modulated the output pattern of the LTC3588-1. During output preparation, the undervoltage-lockout mode allows charges to build up on the capacitor until the buck converter of LTC3588-1 can transfer the charge to the output. During the power-up, the LTC3588-1 automatically sleeps, and its input and output quiescent currents are pretty low at this time. The buck converter will turn on or off as needed to keep the output voltage at a stable interval.

Although DcPMT can provide continuous and stable DC voltage output when wind resources and energy storage are abundant, as an energy device for field applications, it needs to be designed to cope with extreme environmental conditions where wind resources are scarce for long periods of time. Therefore, DcPMT provides an intermittent power supply mode for the sensor in the case of low wind power for a long period of time and insufficient energy storage. The voltage waveforms of DcPMT feeding a $100 \text{ k}\Omega$ load in intermittent supply mode are shown in Figure 5h, and the current is also displayed in Figure S11, Supporting Information. It is easy to see that the output voltage of DcPMT in intermittent power supply mode varies periodically, with the voltage decaying from about 3 V in each cycle, and after a period of time the voltage will return to

3 V again and enter the next power supply cycle. It can be seen that the power supply cycle is affected by the wind speed. When the wind speed is 7.9 m s^{-1} , the load could be powered every 5 s. As the wind speed decreases, the power supply cycle gradually increases. When the wind speed decreases to 4 m s^{-1} , it takes 30 s for the DcPMT to finish a supply cycle. The load current changes with the same period as the voltage. As the wind speed increases, the period of supply becomes shorter and the average value of current increases. From the fluctuations of the curves in Figure 5e,f,h, it can be derived that when the DcPMT is connected to an external load, the charging and discharging will gradually maintain a dynamic balance. Therefore, unlike the charging voltage in the open circuit case, the charging voltage in the on-load case will not always be maintained at a high level so that the diode D_2 in Figure 5a cannot be switched on. In fact, according to Figure S10, Supporting Information, the diodes D_1 and D_2 are passively switched on in turn, depending on the relative magnitude of the output contribution of the TENG and the EMG, especially in a wide wind speed range.

2.5. Demonstration

To demonstrate the performance of TEHG for wind energy harvesting and driving sensors, Figure 6a shows a TEHG-based self-powered sensing system consisting of a hermetically sealed TEHG, a DcPMT, and a sensor module (GY-39). The proposed TEHG provides energy to sensors in the power grid by efficiently harvesting wind energy, which synthetically demonstrates the complementary environmental friendliness associated on the scale from the nano-energy to the large-scale energy, and represents a forward-looking example of clean energy implementation. The sensor module GY-39 is a low-cost micropower sensor which is widely used in IoTs, weather monitoring, and smart farm climate monitoring. It can monitor environmental information such as air pressure, temperature, humidity, altitude, and light intensity. GY-39 supports serial communication, and also can perform power-down hold on data or send through WIFI module. Furthermore, an axial blower is used to simulate the ambient wind energy and a laptop computer is used as a central controller to parse the sampled data transmitted through the serial port and display it simultaneously and visually. Moreover, the demonstration of the GY-39 acquisition of environmental signals driven by the TEHG-based self-powered system is shown in the Movie S4, Supporting Information. Under the switching wind speed of 7 m s^{-1} where the efficiency contributed by the TENG and the EMG modules are comparable and are both higher than 30% (in Figure S10b, Supporting Information), the DcPMT can continuously drive the GY-39 for 2–3 min after about 10 min charging. The effectiveness and stability of the power supply can be reflected by the working condition of the sensor. Figure 6b[i–iii] shows the changes of the sampling results before and after the sensor was covered. In the initial conditions (Figure 6b[i]), the ambient light intensity monitored by the sensor was 132.00 lux. As the experimenter approached and gradually covered the sensor (Figure 6b[ii]), the ambient light intensity monitored by the GY-39 was refreshed and gradually decreased. When the sensor was completely covered (Figure 6b[iii]), the monitored light intensity was 3.60 lux.

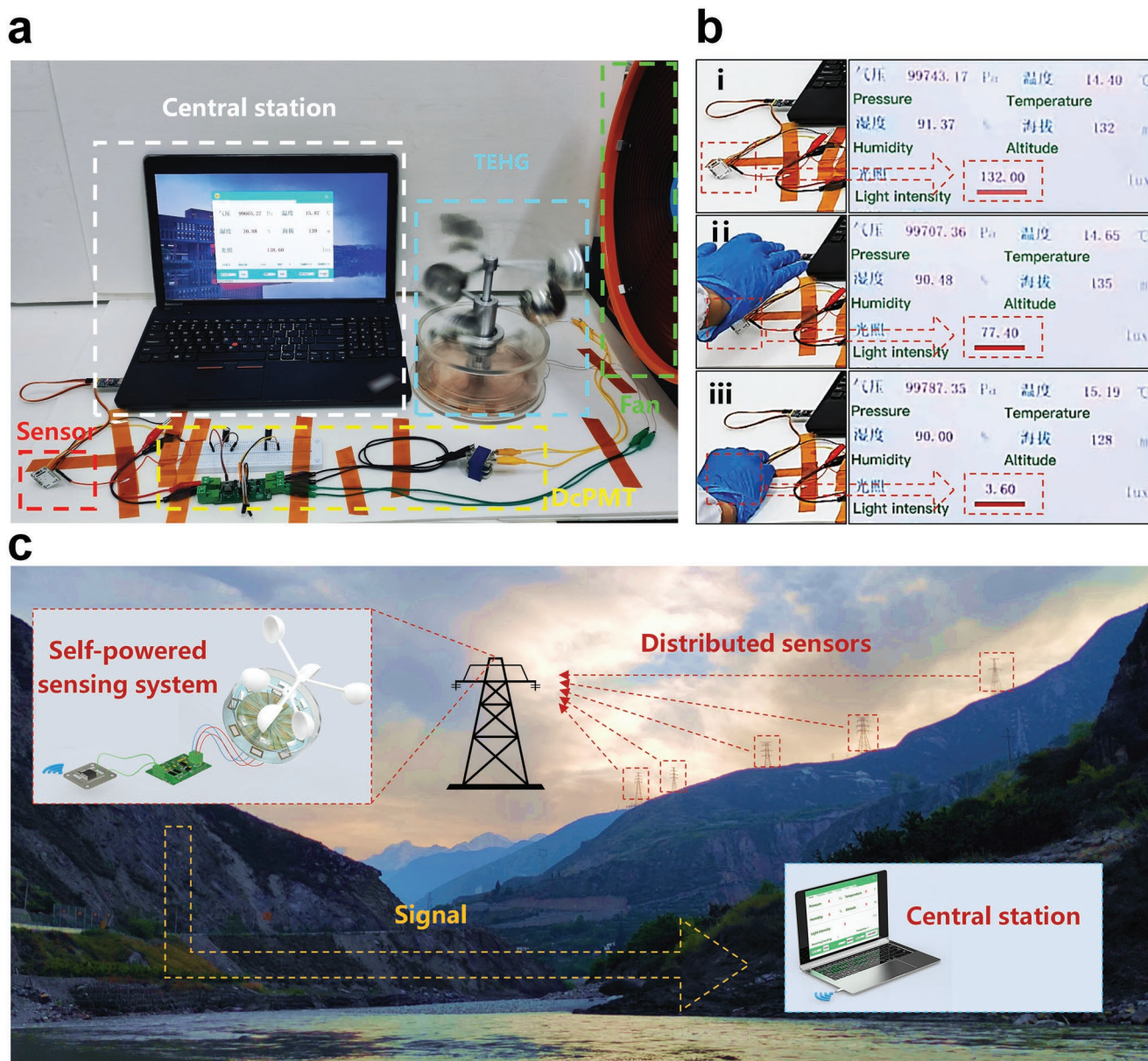


Figure 6. Application test of TEHG-based self-powered system. a) TEHG application test platform built with GY-39 weather module and its b) test results. c) Schematic diagram of TEHG-based self-powered system in smart grid.

During the demonstration, the sensor monitoring results were kept up to date in real time with a follow-up rate of less than 1 s, demonstrating the good working condition of the sensor module under TEHG power supply. Figure 6c demonstrates how this self-supply sensing system works in the smart grid. The sensing systems are installed on transmission towers to collect climate and environmental information along the power transmission line. Each sensing system has a TEHG and DcPMT to collect and manage the abundant environmental energy in the field. This energy drives the sensors to collect environmental information and store or transmit it via a WIFI module. Ultimately, this information is received and parsed by a central controller, and the environmental conditions and oper-

ating conditions of the transmission line are thus controlled. The triboelectric material in the TEHG has good anti-friction properties and maintains electrical characteristics consistent with the initial state after long periods of operation, which facilitates the continuous reliability of the TEHG in the complex environment of the outdoor grid, as depicted in Figure S12, Supporting Information. Generally speaking, TEHG has the advantages of small size, simple structure, easy manufacturing, and cheap price, which makes it easy to be mass produced and installed on a large number of transmission towers. At the same time, due to its wide wind speed and high efficiency wind energy harvesting characteristics, it can be easily activated and harvest the wind energy from the natural environment

in a durable and efficient manner. Furthermore, the DcPMT designed for the TEHG allows the output of electrical energy to be standardized to a typical voltage of 1.8–3.6 V, ensuring the stability of the sensor energy supply.

3. Conclusion

In summary, a TEHG-based self-powered system incorporating a DcPMT with high energy conversion efficiency for wide wind speeds is demonstrated in this work. The efficient energy collecting spectrum is expanded by hybridizing a TENG with an EMG, and the coaxial multi-layered dual-rotation structure design in the TEHG enables the TENG module to start rapidly at slow wind speeds while maintaining the high energy conversion efficiency by the EMG module in strong winds. This paper further investigates the effects of wind cup diameter and rotating arm length on the aerodynamic performance of the TEHG to optimize complementary pairings of the TENG and the EMG in terms of start-up wind speed and dynamics performance. Moreover, the influence of composite forms, the vertical-hybrid, and the lateral-hybrid on the waveform and amplitude of the TEHG output signals were compared and analyzed, and the vertical-hybrid TEHG was finally selected due to its higher and more stable voltage. For the purpose of the optimization toward hybrid harvesting switching intervals in relation to smoother output power curves, the numeration of pole pairs of the TEHG were then studied. Following the above structural optimization, the TENG can produce a 0.12–5.2 mW output power with increasing wind speed from 2 to 16 m s⁻¹, while the EMG contributes a 0.1–12 mW output power in the 4–16 m s⁻¹ wind speed range. Notably, the TENG is the dominant output contributor of the hybrid generator within the slow wind speed region (<5 m s⁻¹), which accounts for 70–100% of the total output, meanwhile the EMG output power contribution is less than 30% at low wind speeds. When the wind speed exceeds 7 m s⁻¹, the EMG gradually becomes the main (50–70%) output component of the TEHG. Through the synergy between the two generating units, the TEHG can maintain an instantaneous energy conversion efficiency of about 40–50% over a wide wind speed range of 2–11 m s⁻¹ with a maximum power density of 41.05 W m⁻³, demonstrating a wide wind speed and high efficiency wind energy collection and conversion capability. Furthermore, a DcPMT is designed and integrally fabricated on single-board to modulate the AC voltage outputs of the TEHG from two separate channels. Owing to the hierarchical topology design that combines isolated energy storage with the undervoltage-lockout strategy, the electrical energy converted by the TEHG can be efficiently stored and converted to a typical DC voltage of 3.3 V to supply electronic sensors. A commercial meteorological monitoring module was chosen to demonstrate the application of the TEHG-based self-powered system. The meteorological module can be driven continuously for 2–3 min under 7 m s⁻¹ wind speed, and the refresh time of the monitoring data is less than 1 s, which could be sufficient for the field IoT scenarios. This work paves an effective and high-efficiency harvesting approach for broadband wind energy, for further potential applications in the environmental self-adaptive and more flexible IoT.

4. Experimental Section

Fabrication of TEHG: As shown in Figure 1b, the fabricated wind energy harvesting system consisted of two main components, that is, from top to bottom, the double rotating shaft wind cups that consisted of two sets of wind cups with varied arm lengths, and a hybrid power generation module that contained a TENG and an EMG. For the double rotating shaft wind cups of TEHG fabrication, a solid aluminum alloy swivel shaft of 20 cm in length and 1.8 cm in diameter and another hollow aluminum alloy swivel shaft of 10 cm in length and 3.2 cm in diameter were machined, and the solid swivel shaft was fixed inside the hollow shaft using insulated bearings to form a concentric double swivel structure. Next, a 0.8 cm diameter, 6 cm long aluminum alloy bracket was fixed at one end of each of the three 6 cm diameter hollow hemispherical aluminum cups, and the other end of the bracket was fixed to the top of the solid rotating shaft, so that the distance from the center of the cup to the rotating shaft was 9 cm. Thus, a 6 cm diameter, 9 cm rotating radius wind cup was made. The other 6 cm diameter aluminum cup was fixed to one end of three aluminum brackets of 0.8 cm diameter and 3 cm length, and the other end was fixed to the top of the hollow rotating shaft to make another cup with 6 cm arm length. Finally, the two concentric double rotating cups were mounted on the upper surface of the insulated housing with insulated bearings, so that the bottom of the solid rotating shaft was connected to the TENG rotor and the bottom of the hollow rotating shaft was connected to the EMG rotor. For the hybrid power generation module of TEHG fabrication, it consisted of three parts: the TENG rotor, the EMG rotor, and the stator disc. For the fabrication of the TENG rotor, an acrylic disc consisting of 12 sector-shaped units with a 15° circular angle and 6 cm radius arranged at the same circular angle interval was cut by a laser cutting machine, and then a FEP film was fixed on both sides of each sector-shaped unit so that the film could naturally arch down and contact the stator. For the fabrication of the EMG rotor, a circular acrylic plate with an inner diameter of 12 cm and an outer diameter of 16 cm was first cut out with a laser cutter as the support structure of the rotor. Eight 20 mm × 10 mm rectangular holes with symmetrical circle centers were cut out of the ring, and eight rectangular strong magnets of the same size were embedded into each hole so that the bottom of the magnet block was flush with the bottom of the rotor disk. The polarity of the magnets should be noted during the insertion of the magnet blocks, making sure that the adjacent blocks were placed in opposite polarity. Finally, for the stator, two compartments were divided on the 16 cm diameter acrylic disc. The inner zone was a 12 cm diameter circle where copper foil was pasted for the TENG electrode. The copper foil was insulated by etching grooves on the surface of the copper foil, and 24 sector electrode units were etched at an angle of 15° to the center of the circle, where the adjacent units were insulated from each other and the inter-sector units were connected by a spoke on one side, thus forming two graphically complementary sector electrode networks. The outer interval of the stator was circular in shape. Eight circularly symmetrical rectangular holes were cut in the circular interval, and a 200-turn rectangular copper coil was set in each hole, the top of which should be flush with the top of the rotor disk. The distance between the rotor and the stator was properly adjusted during installation so that the FEP film of the TENG rotor could just completely cover one sector of the electrode network on the stator without touching the other network. In addition, a gap of about 1 mm between the bottom of the EMG rotor and the stator was maintained to avoid collision during rotation.

Electrical Output Measurements: For the purpose of performance evaluation, the open-circuit voltage and short-circuit current of the TEHG device were measured by a Keithley 6514 system electrometer. For the multichannel measurement and demonstration, the voltage outputs were measured by an ADC (NI 9220, 16-channel voltage measurement module, ±10 V, National Instrument).

Supporting Information

Supporting Information is available from the Wiley Online Library or from the author.

Acknowledgements

S.Y., H.W., and Z.L. contributed equally to this work. This research was supported by the National Natural Science Foundation of China (Grant No. 52007019).

Conflict of Interest

The authors declare no conflict of interest.

Data Availability Statement

The data that support the findings of this study are available from the corresponding author upon reasonable request.

Keywords

broad-band wind energy, nanogenerators, power management circuits, self-powered systems, triboelectric-electromagnetic hybrids

Received: July 20, 2022
Revised: August 30, 2022
Published online:

-
- [1] L. Xie, X. Chen, Z. Wen, Y. Yang, J. Shi, C. Chen, M. Peng, Y. Liu, X. Sun, *Nano-Micro Lett.* **2019**, *11*, 39.
- [2] J. Li, C. Wu, I. Dharmasena, X. Ni, W. Ding, *Intell. Converged Networks* **2020**, *1*, 115.
- [3] T. Li, H. Fan, J. García, J. M. Corchado, *Inf. Fusion* **2019**, *51*, 233.
- [4] L. Atzori, A. Iera, G. Morabito, *Comput. Networks* **2010**, *54*, 2787.
- [5] Z. Ren, X. Liang, D. Liu, X. Li, J. Ping, Z. Wang, Z. L. Wang, *Adv. Energy Mater.* **2021**, *11*, 2101116.
- [6] U. Farooq, N. Tariq, M. Asim, T. Baker, A. Al-Shamma'a, *J. Parallel Distrib. Comput.* **2022**, *162*, 89.
- [7] X. Li, Y. Cao, X. Yu, Y. Xu, Y. Yang, S. Liu, T. Cheng, Z. L. Wang, *Appl. Energy* **2022**, *306*, 117977.
- [8] K. P. Seng, L. Ang, E. Ngharamike, *Int. J. Distrib. Sens. Networks* **2022**, *18*, 155014772110628.
- [9] G. K. Ijamaru, K. L. M. Ang, J. K. P. Seng, *Int. J. Distrib. Sens. Networks* **2022**, *18*, 155014772110677.
- [10] Y. Wu, Q. Zeng, Q. Tang, W. Liu, G. Liu, Y. Zhang, J. Wu, C. Hu, X. Wang, *Nano Energy* **2020**, *67*, 104205.
- [11] H. Shao, P. Cheng, R. Chen, L. Xie, N. Sun, Q. Shen, X. Chen, Q. Zhu, Y. Zhang, Y. Liu, Z. Wen, X. Sun, *Nano-Micro Lett.* **2018**, *10*, 198.
- [12] G. Liu, J. Chen, Q. Tang, L. Feng, H. Yang, J. Li, Y. Xi, X. Wang, C. Hu, *Adv. Energy Mater.* **2018**, *8*, 1703086.
- [13] Q. Zeng, Y. Wu, Q. Tang, W. Liu, J. Wu, Y. Zhang, G. Yin, H. Yang, S. Yuan, D. Tan, C. Hu, X. Wang, *Nano Energy* **2020**, *70*, 104524.
- [14] P. Lu, H. Pang, J. Ren, Y. Feng, J. An, X. Liang, T. Jiang, Z. L. Wang, *Adv. Mater. Technol.* **2021**, *6*, 2100496.
- [15] C. Jung, D. Schindler, *Sustainable Energy Technol. Assess.* **2020**, *42*, 100852.
- [16] C. Rodrigues, C. Alves, J. Puga, A. Pereira, J. Ventura, *Nano Energy* **2016**, *30*, 379.
- [17] F. Fan, Z. Tian, Z. Wang, *Nano Energy* **2012**, *1*, 328.
- [18] W. Wang, J. Xu, H. Zheng, F. Chen, J. Kory, Y. Wu, H. Wang, W. Zhang, R. Yang, *Nanoscale* **2018**, *10*, 14747.
- [19] Y. Zi, H. Guo, Z. Wen, M. Yeh, C. Hu, Z. L. Wang, *ACS Nano* **2016**, *10*, 4797.
- [20] J. Wang, L. Pan, H. Guo, B. Zhang, R. Zhang, Z. Wu, C. Wu, L. Yang, R. Liao, Z. L. Wang, *Adv. Energy Mater.* **2019**, *9*, 1802892.
- [21] Y. Wu, S. Kuang, H. Li, H. Wang, R. Yang, Y. Zhai, G. Zhu, Z. L. Wang, *Adv. Mater. Technol.* **2018**, *3*, 1800166.
- [22] H. Guo, Z. Wen, Y. Zi, M. Yeh, J. Wang, L. Zhu, C. Hu, Z. L. Wang, *Adv. Energy Mater.* **2016**, *6*, 1501593.
- [23] L. B. Huang, W. Xu, G. Bai, M. C. Wong, Z. Yang, J. Hao, *Nano Energy* **2016**, *30*, 36.
- [24] J. Wang, Z. Wu, L. Pan, R. Gao, B. Zhang, L. Yang, H. Guo, R. Liao, Z. L. Wang, *ACS Nano* **2019**, *13*, 2587.
- [25] L. Pan, J. Wang, P. Wang, R. Gao, Y. C. Wang, X. Zhang, J. Zhou, Z. L. Wang, *Nano Res.* **2018**, *11*, 4062.
- [26] Y. Zhong, H. Zhao, Y. Guo, P. Rui, S. Shi, W. Zhang, Y. Liao, P. Wang, Z. L. Wang, *Adv. Mater. Technol.* **2019**, *4*, 1900741.
- [27] L. Gao, S. Lu, W. Xie, X. Chen, L. Wu, T. Wang, A. Wang, C. Yue, D. Tong, W. Lei, *Nano Energy* **2020**, *72*, 104684.
- [28] P. Wang, L. Pan, J. Wang, M. Xu, G. Dai, H. Zou, K. Dong, Z. L. Wang, *ACS Nano* **2018**, *12*, 9433.
- [29] B. Zhang, S. Zhang, W. Li, Q. Gao, D. Zhao, Z. L. Wang, T. Cheng, *ACS Nano* **2021**, *15*, 20278.
- [30] C. Ye, K. Dong, J. An, J. Yi, X. Peng, C. Ning, Z. L. Wang, *ACS Energy Lett.* **2021**, *6*, 1443.
- [31] J. Luo, Z. L. Wang, *Energy Storage Mater.* **2019**, *23*, 617.
- [32] S. Niu, X. Wang, F. Yi, Y. Zhou, Z. L. Wang, *Nat. Commun.* **2015**, *6*, 8975.
- [33] Y. Zi, J. Wang, S. Wang, S. Li, Z. L. Wang, *Nat. Commun.* **2016**, *7*, 10987.
- [34] G. Cheng, H. Zheng, F. Yang, L. Zhao, M. Zheng, J. Yang, H. Qin, Z. Du, Z. L. Wang, *Nano Energy* **2018**, *44*, 208.
- [35] J. Wang, W. Ding, L. Pan, C. Wu, H. Yu, L. Yang, R. Liao, Z. L. Wang, *ACS Nano* **2018**, *12*, 3954.
- [36] H. Wang, J. Wang, R. Liao, L. Yang, H. Wu, Z. L. Wang, *Adv. Funct. Mater.* **2021**, *31*, 2103463.
- [37] H. Luo, H. Wang, L. Yang, H. Wu, S. Kang, S. Yong, R. Liao, J. Wang, Z. L. Wang, *Adv. Funct. Mater.* **2022**, *32*, 2200862.